GDCh
Research Article
Angewandte International Edition Chemie
www.angewandte.org

How to cite: *Angew. Chem. Int. Ed.* **2025**, *64*, e202507967
doi.org/10.1002/anie.202507967

**Li-O$_2$ Batteries** **Hot Paper**

# Discharge Rate-Driven $Li_2O_2$ Growth Exhibits Unconventional Morphology Trends in Solid-State Li-O$_2$ Batteries

*Xiaozhou Huang, Matthew Li,* Yanan Gao, Moon Gyu Park, Shoichi Matsuda, and Khalil Amine**

**Abstract:** Solid-state lithium oxygen batteries (LOBs) are known for their enhanced safety, higher electrochemical stability, and improved energy density compared to liquid-state LOBs. However, the investigation of solid-state LOBs is limited with little understanding of their discharge and charge processes. In this work, a polymer-based solid-state LOB is used to investigate the effect of discharge rate on lithium peroxide ($Li_2O_2$) formation, the oxygen evolution reaction (OER), and cycle performance. Notably, we observe a counterintuitive trend: $Li_2O_2$ particle size increases with increasing discharge current density, in contrast to liquid systems. This behavior arises from inherent space charge layers that restrict $Li^+$ transport under high current, and spatially heterogeneous active sites at the solid electrolyte–cathode interface, directly evidenced by small angle X-ray scattering (SAXS), which govern nucleation accessibility and promote site-selective $Li_2O_2$ growth. Furthermore, higher current densities improve ORR and OER efficiency but accelerate anode degradation, while lower currents promote side reactions. These opposing effects result in a trade-off that defines an optimal discharge rate (0.1 mA cm$^{-2}$) for maximizing cycle life. This study provides a new mechanistic perspective on discharge-driven processes in solid-state LOBs and offers practical guidelines for performance optimization in future high-energy battery systems.

## Introduction

Lithium-oxygen batteries (LOBs) have garnered significant attention as a next-generation energy storage technology due to their remarkable theoretical energy density (3.5 kWh kg$^{-1}$), making them critical for high-energy applications such as aviation, where mass and specific energy requirements exceed the capabilities of traditional lithium-ion batteries.[1–6] This remarkable energy density arises from the electrochemical reaction between lithium and oxygen gas, producing lithium peroxide ($Li_2O_2$) as the main discharge products.[7] Though promising, the current LOBs still suffer from multiple challenges that hinder their practical application, such as large overpotentials, electrolyte instability, and poor cyclability.[8–10]

One of the critical factors affecting the performance and reversibility of LOBs is the morphology of $Li_2O_2$ discharge product. The formation and decomposition of $Li_2O_2$ at the cathode determine the round-trip efficiency, rate capability, and long-term stability. In liquid-state systems, the relationship between discharge rate and $Li_2O_2$ morphology has been extensively studied. Griffith et al. demonstrated that higher discharge current densities lead to smaller $Li_2O_2$ particles, accompanied by a decrease in capacity.[11] The relationship between capacity and rate can be explained by the reduced penetration depth of $O_2$ into the cathode at elevated discharge rates, which can be associated with the smaller particles blocking $O_2$ transport pathways, limiting $Li_2O_2$ growth. Horstmann et al. conducted nanoscale continuum modelling of the discharge process in LOB and also found that an increase in discharge rate tended to increase coverage of $Li_2O_2$ on cathode surface and with smaller particles.[12] The morphologies of $Li_2O_2$ is strongly affected by discharge rates. In some cases, at low discharge rates, $Li_2O_2$ is predominantly found with a toroidal morphology, maintaining a relatively constant average radius. At the higher rates, the $Li_2O_2$ particles transition into a needle-like shape.[11] Li et al. observed that as the discharge rate increases, the $Li_2O_2$ morphology transitions from nanorods to toroidal structures composed of aggregated nanosheets.[13] Xia et al. found that excessive current (−1 mA cm$^{-2}$) could suppress $Li_2O_2$ formation entirely due to rapid carbon surface

---

[*] X. Huang, M. Li, K. Amine
Chemical Sciences and Engineering Division, Argonne National Laboratory, 9700 S Cass Ave, Lemont, IL 60439, USA
E-mail: matthew.li@anl.gov
amine@anl.gov

Y. Gao, S. Matsuda
Center for Green Research on Energy and Environmental Materials, National Institute for Materials Science, 1-1 Namiki, Tsukuba, Ibaraki 305-0044, Japan

M. G. Park
Materials Science Division, Argonne National Laboratory, 9700 S Cass Ave, Lemont, IL 60439, USA

S. Matsuda
SoftBank-NIMS Advanced Technologies Development Center, National Institute for Materials Science, 1-1 Namiki, Tsukuba, Ibaraki 305-0044, Japan

Additional supporting information can be found online in the Supporting Information section passivation.[14] Mitchell et al. revealed that low discharge rates lead to $Li_2O_2$ particles initially forming as stacked thin plates that evolve into toroids through secondary nucleation, whereas high discharge rates promote dense nucleation of equiaxed particles, resulting in less-defined disc and toroid structures.[15] More recent studies often involve complex cathode structures or catalytic surfaces, which though improving performance, introduce additional variables that can obscure the intrinsic relationship between discharge rate and $Li_2O_2$ morphology. A comprehensive review by Liu et al. further summarizes how current density and depth of discharge affect $Li_2O_2$ growth modes, emphasizing that morphological control is key to optimizing battery reversibility and energy efficiency.[16] It is important to note that $Li_2O_2$ morphology is also influenced by the electrolyte composition and the cathode's surface conditions.[17]

Although this relationship has been extensively explored in liquid-state Li-$O_2$ batteries (LOBs), the correlation between discharge rate and $Li_2O_2$ morphology remains rather unexplored in solid-state LOB systems.[18,19] It remains unclear how the varying morphological or dimensional characteristics of $Li_2O_2$ impact the oxygen evolution reaction (OER) and how they influence the cycling performance of the solid-state LOB.[20–24] Compared with liquid-state LOB systems, solid-state LOB systems exhibit distinct characteristics in terms of interfacial impedance, $Li^+$-ion conductivity and $Li^+$-ion diffusion pathway.[25] These differences may result in an unique influence of the discharge rate on the morphology of $Li_2O_2$, discharge-charge profile, and the cycle performance of LOBs. Understanding the interplay between these metrics is crucial towards optimizing LOB battery cycled in solid-state electrolytes.

Among the different types of solid-state electrolytes, polymer-based systems have emerged as the dominant choice for solid-state LOBs in recent years. In our recent comprehensive review of the literature from 2009 to 2024,[20] we found that polymer electrolytes have been increasingly adopted since 2016, and now constitute the majority of reported solid-state LOB systems. This growing preference reflects not only their favorable electrochemical and mechanical properties but also their better compatibility with the unique electrode architecture of LOBs. Specifically, the cathodes in LOBs are typically composed of porous carbon materials to facilitate oxygen diffusion and $Li_2O_2$ deposition. Polymer electrolytes, due to their soft, conformable nature, can achieve intimate interfacial contact with such porous structures—an essential factor for stable electrochemical performance and reproducible morphology studies. In contrast, rigid ceramic electrolytes often suffer from poor contact with porous electrodes, leading to high interfacial resistance and less controlled nucleation behavior. These considerations make polymer-based solid electrolytes a particularly suitable platform for investigating discharge-rate-dependent processes in solid-state LOBs.

To enable mechanistic insights that are broadly applicable, this study employs a composite SSE composed of PVDF-HFP, LiTFSI, and LLZTO. These materials have been widely adopted and thoroughly studied in the field. Our recent comprehensive review of literature from 2009 to 2024 confirms that these components are among the most frequently used in solid-state Li-$O_2$ systems.[20] This choice not only ensures general relevance and reproducibility of the results but also avoids complications associated with the instability of less established materials in Li-$O_2$ system. Specifically, PVDF-HFP is an excellent matrix material due to its relatively high ionic conductivity at room temperature and wide electrochemical stability window (exceeding 5 V versus Li/$Li^+$).[26] In contrast, other commonly used polymer, such as PEO, is only stable below 4.5 V,[27] which may limit its applicability in high-voltage systems like LOBs. In addition, PVDF-HFP exhibits sufficient mechanical strength, which is particularly important in solid-state LOBs. During cell assembly, a metal mesh is typically placed on top of the cathode to apply localized pressure, ensuring that the cathode region serves as the primary active area. Without this configuration, the applied pressure may distribute unevenly across the cell, reducing performance. The robust mechanical properties of PVDF-HFP help the electrolyte membrane withstand the applied pressure without being penetrated or damaged by the metal mesh, thereby preventing short-circuiting and improving structural integrity under compression. LiTFSI has also been widely used in LOBs.[20] While $LiClO_4$ is a viable alternative, its discharge capacity is generally lower than that of LiTFSI.[28] LLZTO plays a key role in the composite by enhancing the ionic conductivity, mechanical stability, and processability of the SSE membrane.[29] LLZTO can act as $Li^+$ carriers and serve as interfacial and internal channels for $Li^+$ transportation.[30,31] La atoms in LLZTO can coordinate with N atoms and C═O groups in typical solvent molecules such as DMF, where the N atoms possess high electron density. Acting as Lewis bases, these species can form complexes that promote partial dehydrofluorination within CPEs. This interaction strengthens the bonding between the PVDF matrix, lithium salt, and LLZTO particles. The resulting structural modification significantly enhances the mechanical strength of the SSE membrane, thereby improving its processability and reproducibility.

In this work, we report a counterintuitive correlation between discharge rate and $Li_2O_2$ morphology in solid-state LOBs: the particle size of $Li_2O_2$ increases with increasing discharge current density. This trend stands in sharp contrast to the well-established behavior in liquid electrolyte systems and indicates that discharge product formation in solid-state LOBs follows fundamentally different transport and nucleation dynamics. We attribute this divergence to the formation of space charge layers (SCLs) at the cathode–electrolyte interface, which restrict $Li^+$ transport at less accessible regions under high-current conditions. As a result, the number of electrochemically active nucleation sites decreases at high discharge current densities, favoring the growth of existing $Li_2O_2$ particles over the formation of new ones—opposite to the behavior observed at low current densities. This structural and morphological heterogeneity is supported by SAXS and SEM analyses, which qualitatively align with the proposed mechanism. In addition, we find that the extent of parasitic reactions also depends on the discharge rate, likely due to differences in $LiO_2$ intermediate behavior. Low current densities promote more uniform nucleation but lead to increased side-product formation, whereas high-current densities improve OER/ORR efficiency yet accelerate anode degradation. These competing effects define a unique trade-off in solid-state LOBs, allowing us to identify an optimal discharge current density (0.1 mA cm$^{-2}$) that balances capacity, efficiency, and long-term stability. Altogether, this work establishes a new mechanistic framework for understanding current-dependent behavior in solid-state LOBs, and opens up new possibilities for rational interface engineering and performance optimization in future solid-state energy storage systems.

## Results and Discussion

### Impact of Discharge Rates on the Formation of $Li_2O_2$

Discharge current densities directly influence the morphology of $Li_2O_2$ formed in LOBs, which in turn determines the discharge capacity, reversibility, overpotential, and rate capability of the cells. The morphology of $Li_2O_2$ formed in solid-state LOB was evaluated as a function of different discharge current densities. To ensure the conclusions of this study are broadly applicable, a typical composite polymer electrolyte (CPE) film, composed of PVDF-HFP, LiTFSI, and LLZTO, is chosen for investigation. The front and back optical images of CPE are shown in Figure S1a,b. The SEM images of the front and back sides are shown in Figure S2a. The back side exhibits a smoother surface, making it more suitable for contact with the lithium metal anode to ensure better interfacial contact. In contrast, the front side is rougher, which is advantageous for interfacing with the porous carbon surface of the GDL (Gas diffusion layer), enhancing the connection and minimizing interfacial impedance. When the membrane orientation is reversed, the cell performance is significantly degraded and becomes highly unstable, with large fluctuations and poor reproducibility (Figure S2b). For example, DEMS shows that $O_2$ evolution during the charge process drops to only ∼20% of the theoretical yield, indicating poor reversibility (Figure S2c). These results clearly demonstrate that reversing the membrane orientation leads to unreliable performance due to improper interfacial contact. Figure S1c shows the cross-section of pristine CPE. The structure appears dense and uniform, with a continuous and compact polymer network. The surface exhibits a relatively smooth texture with fine granular features, indicating excellent electrolyte integrity. Figure S1d shows a cycled GDL pressed with CPE. The morphology is more heterogeneous, with visible fibrous structures from the GDL interspersed within the CPE. The polymer electrolyte appears to have infiltrated the GDL, but there are noticeable voids and rougher textures, suggesting a more porous and interconnected network compared to the pristine CPE. Atomic force microscopy (AFM) was conducted under the protection of Ar atmosphere in a glovebox. This was to prevent water absorption by the LiTFSI in the CPE. AFM images in Figure S3 reveal that both CPE and carbon surfaces of GDL are rough, which enhances interconnectivity and electrolyte infiltration. The minimal contrast in phase (related to elasticity of the sample) suggests uniform material distribution, ensuring stable interfaces. This rough surface morphology is beneficial for reducing interfacial impedance and improving overall cell performance. The basic characterizations of SSE are provided and discussed in Figures S4–S7, including structure determination by FTIR, liquid content analysis by TGA (Thermal gravimetric analysis), ionic conductivity measurement by EIS, and rate capability evaluation through a Li | CPE | Li symmetric cell test. The CPE shows sufficient thermal stability for room-temperature operation, with negligible weight loss below 100 °C as indicated by TGA. The addition of LiTFSI and LLZTO slightly reduces the thermal decomposition onset compared to pristine PVDF-HFP, which is consistent with previous literature. However, the overall thermal behavior remains well within the safe margin for Li-$O_2$ battery operation at ambient conditions. It also exhibits high ionic conductivity ($5.34 \times 10^{-4}$ S cm$^{-1}$) and excellent rate capability from 0.05 to 0.4 mA cm$^{-2}$.

The cells were deep discharged at 0.05, 0.1, and 0.2 mA cm$^{-2}$ up to 8.4 mAh cm$^{-2}$. All three cells show stable discharge plateaus up to 6 mAh cm$^{-2}$. The discharge potential decreases with discharge currents, following the voltage relationship of $0.05 > 0.1 > 0.2$ mA cm$^{-2}$ during the early stages of discharge (Figure 1a). However, the voltage relationship shifts to $0.1 > 0.05 > 0.2$ mA cm$^{-2}$ at the end of discharge, suggesting that cells discharged at 0.1 mA cm$^{-2}$ maintain a better balance between $Li_2O_2$ formation and electron transfer, leading to improved discharge performance.

After deep discharge, the discharge product was examined by SEM. As shown in Figure 1c,d, spherical $Li_2O_2$ particles could be clearly observed from all three cells. Similar to previous observations, the SEM beam was destructive to be for $Li_2O_2$ particles and could be degraded by SEM beam, and the degradation of small $Li_2O_2$ was quicker.[32] However, unlike the case in liquid-state LOBs, where toroidal $Li_2O_2$ particles are observed,[17] the $Li_2O_2$ particles formed in the solid-state LOBs are more irregularly shaped. Interestingly, it has been observed that the size of $Li_2O_2$ particles increases with higher discharge rates. Specifically, the average diameters of $Li_2O_2$ particles are measured to be 0.45, 0.74, and 1.2 µm (bimodal distribution centered at around 0.6–0.7 and 1.5 µm) as shown in Figure 1b–d (SEM) and Figure 1e–g (histograms), at discharge rates of 0.05, 0.1, and 0.2 mA cm$^{-2}$, respectively. This trend is opposite to the widely accepted behavior in liquid-state cells, where $Li_2O_2$ particles size typically decreases as the discharge current increases.[11] Griffith et al. indicated that the particle size of $Li_2O_2$ decreases at higher discharge rates due to the rapid supersaturation of discharge product in the electrolyte promoting nucleation rather than growth.[11] Johnson et al indicated that a higher donor number of the solvent increase the $Li_2O_2$ particle size due to the higher stability of $LiO_2$ against disproportionation into $Li_2O_2$.[33]

However, compared to liquid-state LOBs, several factors differ in solid-state LOBs, leading to differing $Li_2O_2$ nucleation and growth behaviors. In liquid-state LOB, $O_2$ and $Li^+$ ions are dissolved in the electrolyte while electrons are transported through the carbon. This configuration only requires a two-phase boundary. In solid-state LOBs, where free solvent does not readily exist, $O_2$ cannot diffuse freely

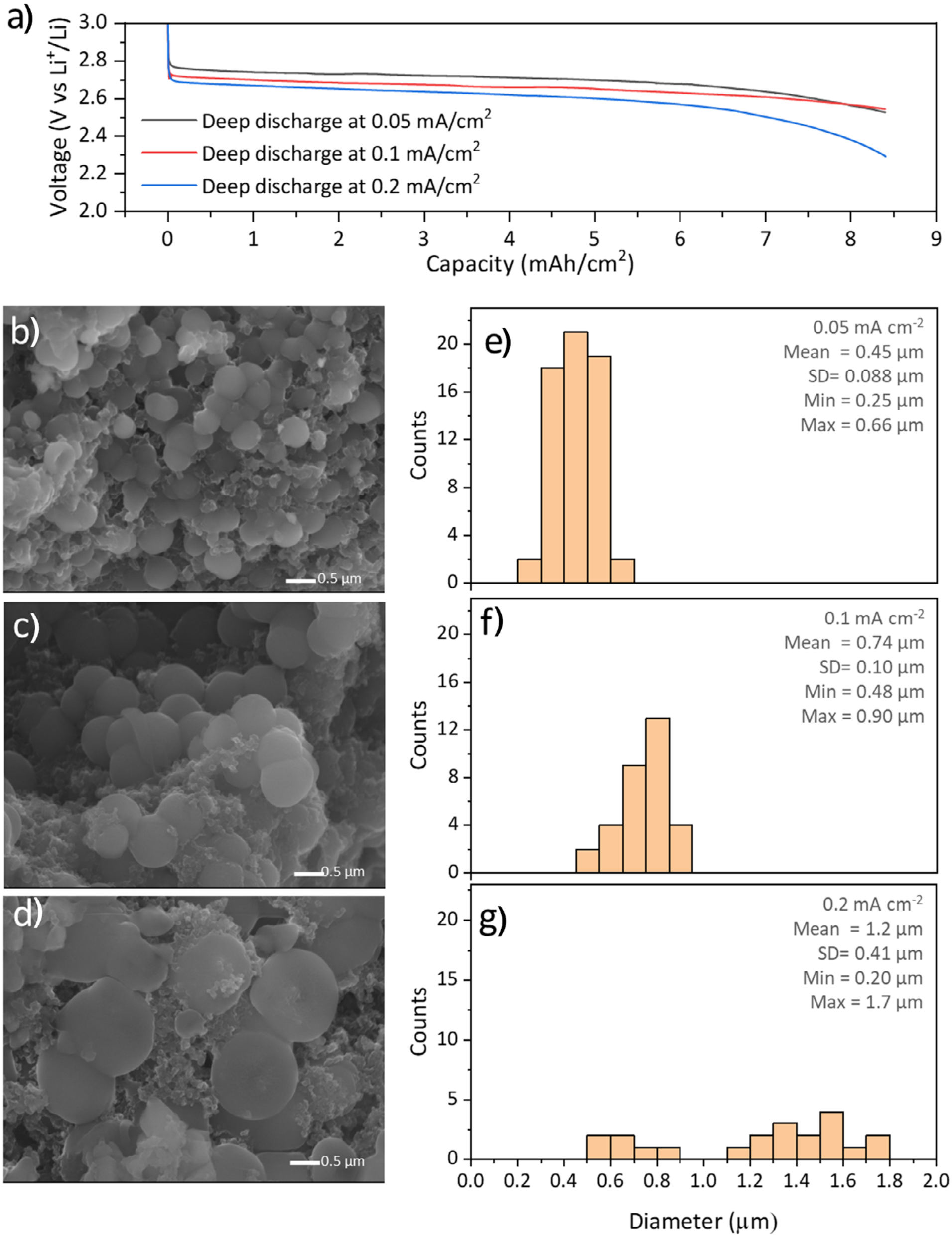

***Figure 1.*** Correlation between discharge current densities and morphology of $Li_2O_2$. a) discharge profiles at different rates. (b-d) Scanning electron microscopy of the morphology of $Li_2O_2$ particle formed at 0.05, 0.1, and 0.2 mA cm$^{-2}$. (e-g) their respective histograms.

in the polymer electrolyte and must rely open pore structure for transport. Therefore, electrochemically active site must involve three phases: $O_2$, $Li^+$ ions and electron transport media. Accordingly, the degree of tortuosity in $O_2$, $Li^+$, and electron transport pathways are likely different from one another suspect that oxygen diffusion pathways might be more selective with a large portion being of lower quality, resulting in a current focusing effect where highly $O_2$ transporting pathways are drastically favored. This leads to the formation of distinct active sites at the SSE–cathode interface, with varying favorability for $Li_2O_2$ nucleation and growth. The presence of such heterogeneous sites is supported by synchrotron small-angle X-ray scattering (SAXS) results, which will be discussed in detail later.

While a similar phenomenon can be claimed in a liquid system as well, a key distinction in solid-state electrolytes lies in the more severe blockage of $O_2$ transport pathways. This is primarily attributed to the formation of a space charge layer (SCL) (Scheme 1), which results from the limited ability of lithium salts to neutralize local charge accumulation, thereby hindering Li-ion transport, especially under high-current densities.[34] At high discharge rates, more $Li^+$ ions accumulate near the interface, strengthening the SCL.[10] The enhanced SCL increases interfacial impedance and hinders the further transport of $Li^+$, $O_2$, and electrons to the active sites. As a result, only a few highly active sites with good transport pathways can sustain growth, leading to the enlargement of existing $Li_2O_2$ particles. Less active

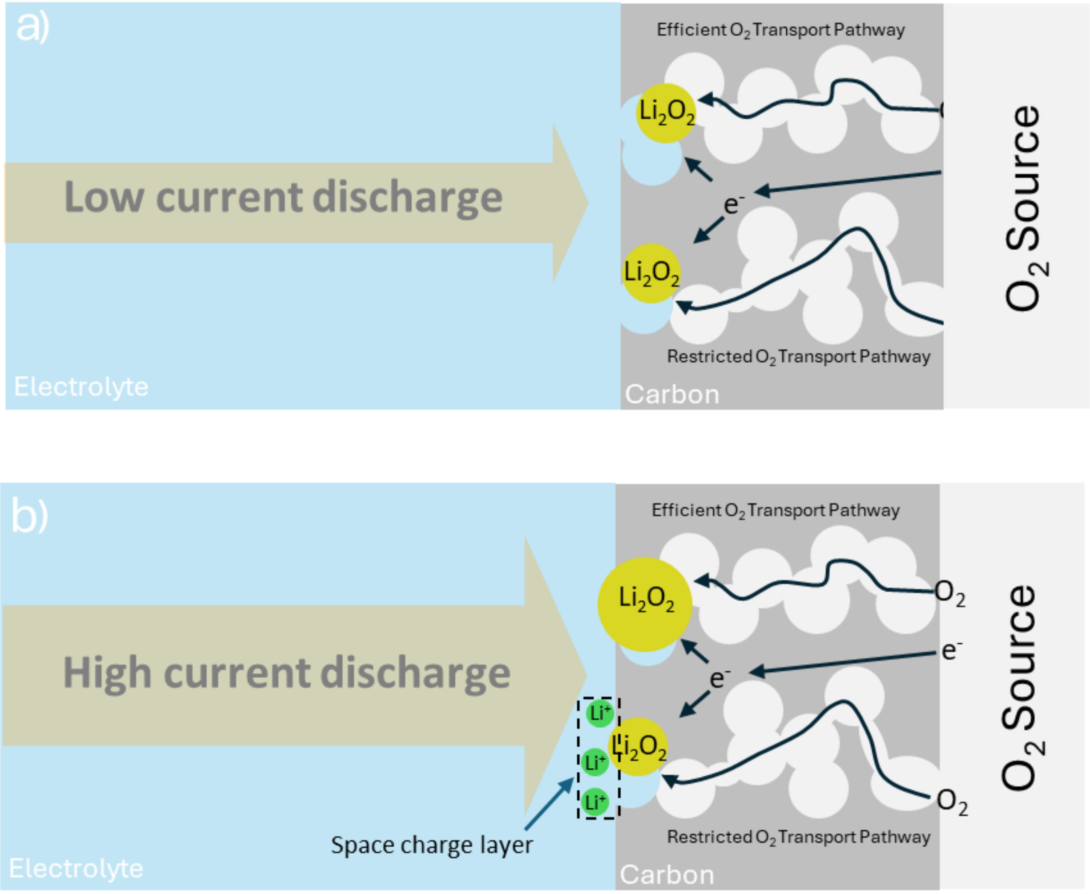

***Scheme 1.*** Growth mechanism of $Li_2O_2$ at different discharge current affected by space-charge layer. a) At low current density the transport of both Li-ion and $O_2$ can be sustained. b) At higher current densities, the mismatch between the $O_2$ and Li-ion transport likely creates a space charge layer-like interface that cannot be neutralized by the polymer electrolyte resulting in Li-ion transport pathways becoming focused to regions where $O_2$ and Li-ion transport can be sustained.

sites suffer from a mismatch of excess $Li^+$ and limited $O_2$, causing passivation and blocking. Therefore, solid-state LOBs under high current tend to favor the growth of existing $Li_2O_2$ rather than the nucleation of new particles. At low rates, due to the lower current, the $Li^+$ repulsion effect from the SCL is weaker, allowing more sites to remain accessible for nucleation. Thus, $Li_2O_2$ formation proceeds through nucleation at multiple sites rather than growth of existing deposits.

This mechanism can be supported by two lines of evidence. First, SEM images reveal that $Li_2O_2$ particles formed under high-discharge-current densities are fewer in number but significantly larger in size, whereas those formed at lower currents are more numerous yet smaller. This trend aligns well with the impact of space charge layers (SCLs), which suppress nucleation at less active sites and promote growth at limited favorable regions. Second, synchrotron SAXS results, which provide direct structural evidence for the existence of distinct favorable sites at the SSE–cathode interface that facilitate or hinder the nucleation and growth of $Li_2O_2$. SAXS technique is a powerful technique for probing the extent and manner in which porous structures are filled or altered by other materials.[35] In our studies, ex situ SAXS data of pristine cathode, pressed cathode and SSE, and cathode filled with DMF solvent were shown in Figure S8. The pore volume distribution as a function of radius is shown in Figure S8b. The scattering vector $q$ is defined as, $q = \frac{4\lambda}{\sin\theta}$ where $\lambda$ is the X-ray wavelength and $\theta$ is the scattering angle. The Pore size $D$ can be estimated by the equation $\mathrm{D} = \mathrm{a} * \frac{2\pi}{\mathrm{q}}$, where a is an empirically determined instrument-specific constant derived from standard calibration samples. Accordingly, smaller $q$ values correspond to larger pore features. The low-$q$ region ($q < 0.03$ Å$^{-1}$) corresponds to large pores, the mid-$q$ region ($0.03$ Å$^{-1} < q < 0.07$ Å$^{-1}$) corresponds to medium-sized pores. high-$q$ region ($q > 0.07$ Å$^{-1}$) is attributed to small pores. In addition, the scattering intensity I is proportional to electron density contrast $\Delta\rho$ difference between matrix material and any substances present within the pores, $\mathrm{I} \propto |\rho_{\text{matrix}-}\rho_{\text{fill}}|$. In our case, the matrix material is porous carbon, while the pore-filling materials include gas (when the pores are empty), solid-state electrolyte (SSE), and DMF liquid solvent.

Compared with pristine cathode (black curve, Figure S8c), the SAXS intensities of cathode/SSE sample (red curve) are lower in both low-$q$ and high-$q$ regions, but remain similar in mid-$q$ region. This indicates that large and small pores are partially or fully filled by the SSE layer, leading to reduced electron density contrast and hence lower scattering intensity. In contrast, the mid-sized pores, particularly around $q = 0.04$ Å$^{-1}$ where the two curves overlap, appear to remain unfilled. The unchanged intensity in this region suggests that the pores are still occupied by argon gas, resulting in no significant change in electron density contrast ($\Delta\rho$) and thus no change in scattering intensity. This result suggests that pores of different sizes are filled by the SSE to varying degrees: some pores are fully filled, others are partially filled, and some remain unfilled (Figure S8d). The volume distribution for the cathode/SSE sample supports the proposed mechanism. The observed decrease in both small and large pore volumes suggests that these pores are occupied by the SSE membrane (Figure S8b). In contrast, the volume distribution of mid-sized pores increases, which may indicate that some large pores are only partially filled by the SSE and now fall within the mid-size range. This partial filling could result in a modest increase in the fraction of mid-sized pores. Additionally, as the volume fractions of small and large pores decrease, the relative contribution of mid-sized pores naturally becomes more significant.

A fundamental design challenge in solid-state LOBs arises from the opposing requirements of achieving intimate SSE–cathode contact and maintaining porous pathways for oxygen transport. On the one hand, high-pressure crimping is often necessary to reduce interfacial impedance by ensuring close contact between the SSE and cathode. On the other hand, excessive pressure can collapse the porous structure required for $O_2$ diffusion. Our SAXS results provide direct structural evidence for this trade-off: pores within the cathode exhibit heterogeneous filling behavior, with some fully filled by the SSE, others partially filled, and some remaining open. This leads to a distribution of interfacial regions with varying accessibility to $Li^+$ and $O_2$, corresponding to active and less active reaction sites. The presence of such spatial heterogeneity supports the proposed mechanism in which SCL further restricts transport at less accessible regions, especially under high discharge currents. The SAXS data, in conjunction with SEM evidence, confirms that solid-state LOBs batteries operate under a site-selective mechanism where SCL strength, pore accessibility, and transport heterogeneity jointly govern the $Li_2O_2$ formation pathway.

Moreover, TGA reveals the presence of residual DMF within the membrane; however, the amount is minimal and does not extend into or fill the porous cathode structure, as confirmed by SAXS results. As shown in Figure S8e, when the porous carbon cathode is fully filled with DMF liquid, the scattering intensities in both the low-q and mid-q regions decrease significantly, indicating that large and medium-sized pores are occupied by the solvent. In contrast, the high-q region remains unchanged, suggesting that small pores are not filled—likely due to the surface tension of DMF, which prevents it from penetrating pores below a certain size. Compared to the cathode/SSE sample, the cathode/DMF sample exhibits much lower scattering intensity, further supporting that in the actual integrated cathode/SSE structure, DMF does not overflow into the cathode to fill all pores. Instead, it remains primarily confined within the membrane. The volume distribution shows a decrease in mid- and large-sized pores, indicating that these pores are filled by the DMF solvent. In contrast, pores with radius smaller than 30 Å remain unfilled, likely due to the inability of DMF to penetrate such small pores as a result of surface tension limitations (Figure S8b).

While the structural and interfacial analyses above explain the site-selective behavior of $Li_2O_2$ formation at the mesoscale, further mechanistic insight can be gained by considering the behavior of $LiO_2$ intermediates at the molecular level. The difference in $LiO_2$ mobility between liquid and solid-state systems introduces an additional layer of control over where and how $Li_2O_2$ forms and grows.

The role of $LiO_2$ intermediates provides key insight into the contrasting behaviors of liquid and solid-state Li-$O_2$ systems. In solid-state systems, $LiO_2$ is essentially insoluble and immobile due to the absence of a liquid phase. It stays fixed at the site where $Li^+$, $O_2$, and electrons meet a true three-phase boundary. The number and quality of such active sites depend on how well the SSE physically contacts the porous cathode, as shown by SAXS. Under low discharge rates, the space charge layer (SCL) effect is relatively weak, allowing $Li^+$ to reach even fewer active sites. This leads to dispersed $Li_2O_2$ nucleation and the formation of small particles at many locations. At high discharge rates, $Li^+$ and $O_2$ fluxes increase, but the SCL effect becomes stronger, limiting $Li^+$ transport to less accessible regions. Since $LiO_2$ cannot diffuse away, it reacts immediately at the few remaining active sites. As the total discharge capacity remains fixed, these sites receive more reactants, resulting in faster local growth and the formation of larger $Li_2O_2$ particles. This morphology shift arises directly from the low solubility and immobility of $LiO_2$, which prevents it from redistributing across the electrode. This rate-dependent $Li_2O_2$ morphology in which low rates yield many small particles while high rates produce fewer but larger ones can be directly confirmed by SEM analysis. In contrast, in liquid-state systems, $LiO_2$ is soluble and mobile. At low current densities, it has time to diffuse before undergoing disproportionation or electron transfer. During this time, $LiO_2$ may be absorbed by pre-existing $Li_2O_2$ deposits, leading to the formation of larger particles. Therefore, low rates in liquid systems tend to yield fewer but larger $Li_2O_2$ particles. At high rates, however, $LiO_2$ has insufficient time to diffuse and instead reacts quickly near its origin, forming localized $Li_2O_2$ deposits that may block the site. Simultaneously, rapid supersaturation promotes widespread nucleation across multiple sites, resulting in a high density of smaller particles.

### Investigation of the Overpotential in Oxygen Evolution Reaction

The OER process of $Li_2O_2$ deposited at different discharge rates were investigated, all three cells were then charged at the same current density of 0.1 mA cm$^{-2}$. The discharge-charge profile is shown in Figure 2a. All cells exhibit a stable plateau during the oxygen reduction reaction (ORR) process. The voltage profiles of all three cells during the charging process exhibit an initial sloped regime followed by a plateaued regime. Overall, the higher the discharge current

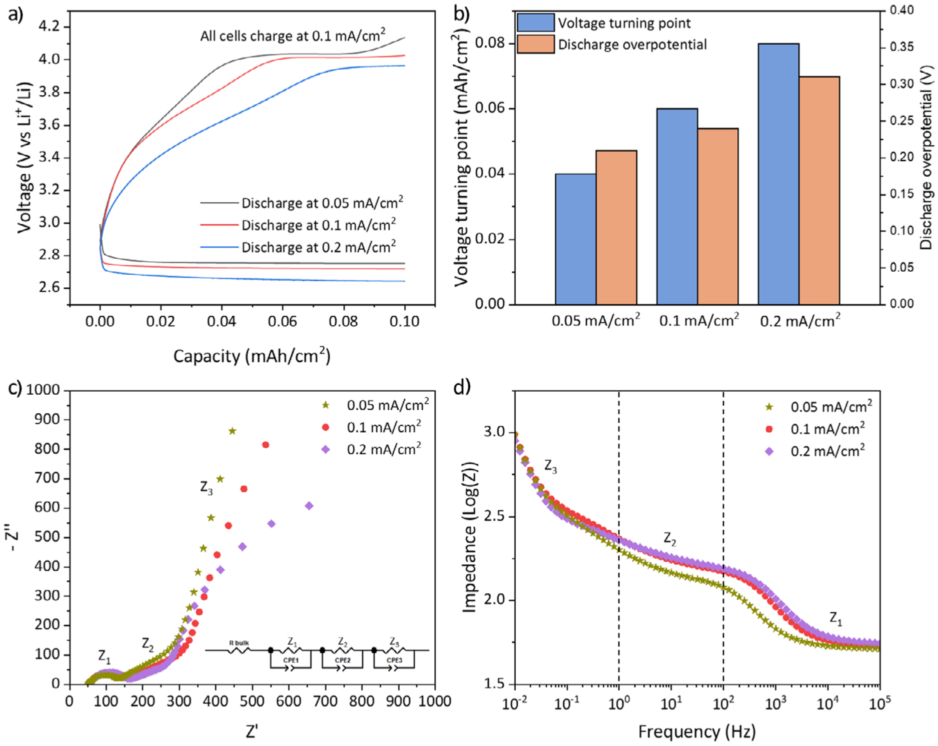

*Figure 2.* The OER overpotential investigation. a) Discharge-charge profile of solid-state LOBs at different discharge rates and same charge rates. b) Bar graph of voltage tuning point of charge step and discharge overpotential of cells operating at different discharge current densities. c) Nyquist plot, and d) Impedance magnitude bode plot of EIS of solid-state LOB cells after discharging at 0.05, 0.1, and 0.2 mA cm$^{-2}$, respectively, up to a capacity of 8 mAh cm$^{-2}$.

density, the lower the charge potential. The capacity upon with the turning points between the initial potential sloped regime and the potential plateau regime are approximately 0.04, 0.06, and 0.08 mAh cm$^{-2}$ for the cells discharged at 0.05, 0.1, and 0.2 mA cm$^{-2}$, respectively (Figure 2b). The discharge capacity was increased to 0.5 mAh cm$^{-2}$, but the charge voltage still follows the same trend as before: higher discharge rate results in lower charge voltage (Figure S9). These discharge-charge profiles do not align with previous studies on liquid-state LOB systems. $Li_2O_2$ that can be oxidized at lower voltages have been previously associated to film-like or nanosized $Li_2O_2$,[36] which is not the case in this study. To understand this unexpected trend, the dQ/dV was calculated to further study the trends in the voltage profile (Figure S10). Two major peaks are observed for all samples, one at low potential (<3.8 V) and the other at a relatively higher potential (>3.8 V), which corresponds to the two different charging regimes in (Figure 2a). The lower potential peak appears to be further composed of two peaks for the cell discharge at 0.1 mA cm$^{-2}$. The cell discharged at 0.2 mA cm$^{-2}$ exhibited the largest peak magnitude followed by 0.1 and then 0.05 mA cm$^{-2}$. However, the potential position of the peak was the lowest for 0.05 mA cm$^{-2}$ (−3.55 V) versus 3.65 and 3.75 V for 0.2 and 0.1 mA cm$^{-2}$, respectively. The cell discharged at 0.05 and 0.1 mA cm$^{-2}$ do indeed appear to have lower first peak position, which could indicate that the smaller particle sizes of $Li_2O_2$ that have been formed at lower current discharge (as found in the SEM in Figure 1b,c) possess a lower charge potential initially and suggests that initially, the charge trends in observed in the liquid system[36] still hold true to some degree. However, the 2nd peak for 0.05 and 0.1 mA cm$^{-2}$ occurs at a higher potential than the 1st peak of 0.2 mA cm$^{-2}$, possibly indicating different $Li_2O_2$ oxidation modes depending on the particle size or impurities.

As the overpotential is associated with both the impedance of the anode and cathode interfaces,[37] investigated it is crucial to first deconvolute the source of the large overpotential. Initial EIS measurements were conducted on all cells. Subsequently, the cells were subjected to deep discharge at current densities of 0.05, 0.1, and 0.2 mA cm$^{-2}$, respectively, up to a capacity of 8 mAh cm$^{-2}$. Following the deep discharge, post-discharge EIS measurements were performed on all cells.

The Nyquist plot and Bode-like plot of three cells are shown in Figure 2c,d, respectively. Three distinct impedance sources, labeled as $Z_1$, $Z_2$, and $Z_3$ from high frequency to low frequency, were identified based on fitting the data to the equivalent circuit shown in in Figure 2c. This circuit consists of a bulk resistor and three parallel combinations of a constant phase element (CPE) and a resistor. Following studies by Adams et al., Landa–Medrano et al, and Højberg et al.' studies, we associate $Z_1$ with the anode and $Z_2$ and $Z_3$ attributed to the cathode.[38–40] $Z_2$ is believed to be a cathode-specific process that is irrelevant to the oxygen reduction, as it could be present in the argon atmosphere.[40] $Z_3$ represents the resistance of the electronic transport through the discharge products, such as $Li_2O_2$.[40] The decrease of impedances associated with the increase of discharge current densities are

*Table 1:* EIS fitting results for solid-state LOB cells discharged at different rates.

| mA cm$^{-2}$ | R bulk | $Z_1$ | $Z_2$ | $Z_3$ |
|---|---|---|---|---|
| 0.05 | 51.4 | 76.04 | 244 | 9482 |
| 0.1 | 53.37 | 96.86 | 241.1 | 3997 |
| 0.2 | 54.73 | 101 | 159.4 | 1416 |

consistent with the charge profile where the charge voltage are also lower in the cell that is discharged at higher current densities (Table 1). Clearly, the impedance of discharge products on cathode surface is higher when they are produced at lower discharge current densities (discharged up to 8.4 mAh cm$^{-2}$) where $Z_3$ was fitted to be 9482, 3997, and 1416 from 0.05, 0.1, and 0.2 mA cm$^{-2}$, respectively and corroborates the overpotentials trends with discharge current density.

From the SEM results, a high discharge rate tends to produce larger $Li_2O_2$ particles, suggesting that larger $Li_2O_2$ particles are more easily oxidized during charging as they exhibit a lower overpotential charge (dQ/dV analysis) and lower impedance. Typically, smaller $Li_2O_2$ particles have a higher surface area relative to their volume (comparatively higher contact area with conductive support and shorter transport path length for Li-ion and electrons than larger particles) and in theory, should facilitate oxidation, leading to a lower overpotential charge.[14,36] The fact that our result indicates larger $Li_2O_2$ particle yield lower OER potential suggest something else is possibly dominating the OER potential. dQ/dV analysis suggests there exist at least three oxidation events stemming from either sufficiently distinct groups of $Li_2O_2$ particle sizes (with differing impedance) or differing degree of impurities arising from parasitic reactions during ORR. Given that the particle size distribution appears to be relatively monomodal (Figure 1d,e) for both 0.05 and 0.1 mA cm$^{-2}$, it is unlikely there is a secondary distribution of $Li_2O_2$ that exists unless they are on order of nanometers and not easily visible by SEM.

Whether the cause of the observed trend in OER overpotential and discharge current density is truly the results of an unseen (by SEM) distribution of $Li_2O_2$ or differences in parasitic reactions can be probed by simply measuring the purity of the discharge product. The yield of $Li_2O_2$ from three carbon paper cathodes discharged at different rates was titrated using a Ti(IV)$OSO_4$ solution. The results indicate that the $Li_2O_2$ yield was 79.8%, 82.3%, and 83.3% for cells discharged at 0.05, 0.1, and 0.2 mA cm$^{-2}$, respectively (Figure S11). This trend suggests that a lower discharge rate leads to a lower $Li_2O_2$ yield, accompanied by an increased side product formation. The side products on cathodes were dissolved in $D_2O$ solution, and the resulting solutions were analyzed using NMR spectroscopy. It is well-established that the main byproducts in LOB systems are lithium formate and lithium carbonate.[41] Lithium formate exhibits a characteristic peak at approximately 8.28 ppm in the $^{1}$H NMR spectrum, while lithium carbonate shows a peak at around 168 ppm in the $^{13}$C NMR spectrum. These peak positions were confirmed using commercial lithium formate and lithium carbonate powders as reference standards (Figure S12c,f). Figure S12a,d show the $^{1}$H and $^{13}$C NMR spectra of the cathode extracts from cells discharged at different current densities. All samples exhibit peaks at −8.28 ppm in the $^{1}$H NMR and −168 ppm in the $^{13}$C NMR, indicating the presence of lithium formate and lithium carbonate, respectively. These peaks match those observed for the commercial reference standards shown in Figure S12c,f. Since all samples were dissolved in the same volume of $D_2O$ and measured under identical conditions and parameters, the intensity of the characteristic peaks can be correlated with the concentration of lithium formate and lithium carbonate. The results show that as the discharge current density increases, the peak intensity at 8.28 ppm in the $^{1}$H NMR and at 168 ppm in the $^{13}$C NMR progressively decreases (Figure S12b,d), confirming that the overall concentration of these byproducts decreases with increasing discharge current density."

Consequently, we believe that the high impedance/overpotential during OER observed in cell discharged under low current densities can be primarily attributed to these byproducts and less likely to be from a multimodal particle size distribution. Differential electrochemical mass spectrometry (DEMS) conducted during OER was also carried out to study the OER efficiency. Cells were discharged to 0.5 mAh cm$^{-2}$ at current densities of 0.05, 0.1, and 0.2 mA cm$^{-2}$ and all charged at 0.1 mA cm$^{-2}$ with the $O_2$ and $CO_2$ quantified by DEMS. The DEMS results of cell discharged at different current densities to 0.5 mAh cm$^{-2}$ are presented in Figure 3. The charge profiles follow the same trend as previously discussed: cells discharged at higher current densities exhibit lower charge voltages, consistent with the earlier observations.

The low OER rate observed at the initial stage of charging is a well-known challenge in LOBs, including solid-state systems. This phenomenon is often attributed to the oxidative decomposition of parasitic byproducts during the discharge process. In our system, lithium formate and lithium carbonate were identified as discharge byproducts (characterization details provided later). Notably, lithium formate decomposes around 3.4 V versus Li/Li$^{+}$,[42] which aligns with the onset of the charging process. The oxidation of these byproducts at the early stage of charging contributes to the suppressed OER rate. Additionally, if the lithium anode is not properly passivated, oxygen consumption from side reactions can further inhibit OER activity. The absence of a liquid electrolyte in solid-state systems exacerbates these effects, leading to a delayed onset of oxygen evolution and a persistently low OER rate in the initial charging phase. Similar behavior has been reported in previous studies, such as Liang et al.,[43] where stronger parasitic reactions in the absence of redox mediators led to significant charging instability and delayed $O_2$ evolution.

Since the capacity is 0.5 mAh cm$^{-2}$ for all cells, which is equivalent to $-9.32*10^{-6}$ mole cm$^{-2}$ of $O_2$ generation based on the reaction $2Li^{+} + 2e^{-} + O_2 \rightarrow Li_2O_2$ can be used to quantify the OER efficiency of each cell. The $Li_2O_2$ DEMS yield rates are 72.7%, 80.7%, and 85.8% for cells discharged at 0.05, 0.1, and 0.2 mA cm$^{-2}$, respectively. Clearly, cells discharged at higher current density have both a higher $Li_2O_2$ yield during ORR (titration result, Figure S11) and a corresponding OER efficiency. Furthermore, the higher

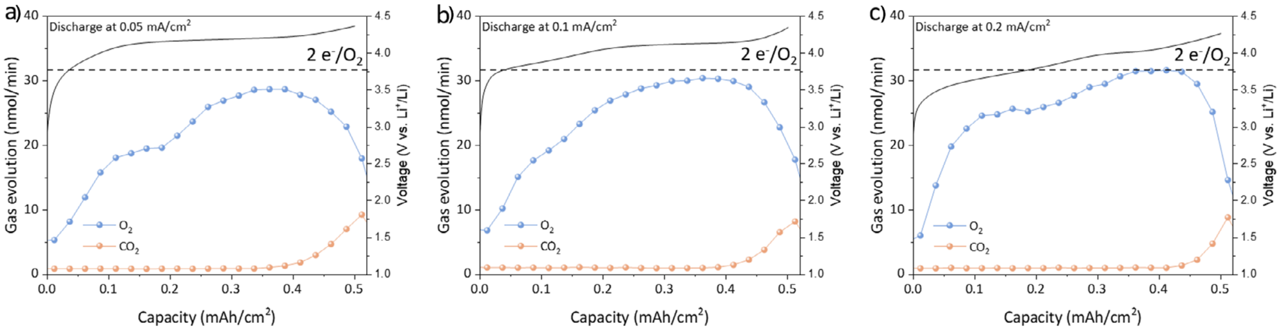

***Figure 3.*** OER DEMS results (at 0.1 mA cm$^{-2}$) for cells discharged at different rates. a) 0.05 mA cm$^{-2}$, b) 0.1 mA cm$^{-2}$, and c) 0.2 mA cm$^{-2}$.

OER yield is not simply due to a higher $Li_2O_2$ yield during ORR. At 0.05 mA cm$^{-2}$ the $Li_2O_2$ yield is 79.8% but the OER $O_2$ yield was only 72.7%, a loss of 7.1% from OER alone. With increasing current density this inefficiency decreases. At an ORR current density of 0.1 mA cm$^{-2}$, the corresponding loss from OER is 1.6%, which is then further reduced to 0.2 mA cm$^{-2}$ to $<$ 0% (i.e., within measurement of titration/DEMS and/or formation) of non $Li_2O_2$ discharge products. The increasing OER efficiency with increasing ORR discharge rate is likely due to a lowering of the charge potential, reducing side reactions. From the DEMS results, these cells evolved 0.651, 0.559, and 0.483 µmol of $CO_2$ gas for discharge rates of 0.05, 0.1, and 0.2 mA cm$^{-2}$, respectively. This confirms that cells discharged at a higher rate tend to generate fewer byproducts, benefiting both ORR, forming more $Li_2O_2$ and the subsequent OER for a more efficient charging process.

To further understand the origin of this improved reversibility and suppressed side reaction behavior, we examined the role of $LiO_2$ intermediates and their nucleation dynamics under different discharge current densities. Discharge current density significantly influences both the activation of nucleation sites and the behavior of $LiO_2$ intermediates at these sites. At low current densities, $LiO_2$ is generated slowly and can disproportionate across a wider range of surface sites due to the weaker electrostatic repulsion from the SCL. This spatially dispersed nucleation leads to lower local $LiO_2$ concentrations and slower disproportionation kinetics. As a result, $LiO_2$ remains at the interface for longer durations and has increased opportunities to participate in parasitic reactions with the surrounding solid electrolyte or cathode components, compromising reversibility. In contrast, at higher current densities, the SCL becomes more intensified and restricts $Li^+$ transport to less favorable regions, effectively localizing electrochemical activity to a limited number of highly active sites where transport remains sufficient. $LiO_2$ accumulates more rapidly at these sites, promoting aggregation and disproportionation into $Li_2O_2$ before significant side reactions can occur. This site-concentrated growth pathway favors the formation of denser and purer $Li_2O_2$ deposits, thereby reducing side product formation. These trends are supported by DEMS results, which show enhanced oxygen evolution at higher current densities, and by SEM observations of fewer but larger $Li_2O_2$ particles under the same conditions.

To further confirm the impact of discharge current density on OER efficiency, we employed a constant voltage discharge where the current versus time profile that the system can sustain is used to test the extreme case of maximally high (at 2.3 V) current density. Cells were first discharged at constant current (1 mA cm$^{-2}$) to 2.3 V in an attempt to eliminate capacitive capacity contribution. Subsequently, cells were held at a reducing potential of 2.3 V versus $Li^+$/Li and the current versus time profile was collected (shown in Figure 4a). During the initial stage of discharge, the current drops rapidly from a very high value, followed by a smaller and stable current. The cells were discharged until capacity reached either 0.3 mAh cm$^{-2}$ (high-current region) or 1.5 mAh cm$^{-2}$ (low current region). High-current region was selected to ensure most of the $Li_2O_2$ capacity stems from high-current density discharge while the low current region has the majority of its $Li_2O_2$ deposition occurring at lower current density (−0.42 mA cm$^{-2}$). Subsequently, both cells underwent OER with gas evolution being monitored by DEMS. The total evolution of $O_2$ gas was quantified and compared with the expected amount based on the capacity obtained during constant voltage discharge (Figure 4b,c). The efficiency of the high-current region was determined to be 85.6%. To isolate the efficiency of the low-current region, the high-current region's capacity and its corresponding higher efficiency contribution were subtracted using Equation S1 and calculated to be 81.6%, indicating a higher OER efficiency than the high-current region and aligning with the constant-current density result (Figure 3). It should be noted that the yield from the potentiostatic discharge appears to be generally lower than the galvanostatic discharge, which we believe stems from a lower discharge potential (2.3 V versus > 2.6 V). Nevertheless, this result further indicates that the tendency for a higher discharge rate to result in less byproducts holds true even at the extreme case of constant voltage discharge with current densities reaching well over 1.8 mA cm$^{-2}$ during the early stages of discharge.

### *Impact of Discharge Rates on Cycle Performance*

To evaluate the impact of discharge rate on cycle performance of solid-state LOBs, cells were made and cycled at discharged current densities of 0.05, 0.1, and 0.2 mA cm$^{-2}$, while maintaining a consistent charge current density of 0.1 mA cm$^{-2}$.

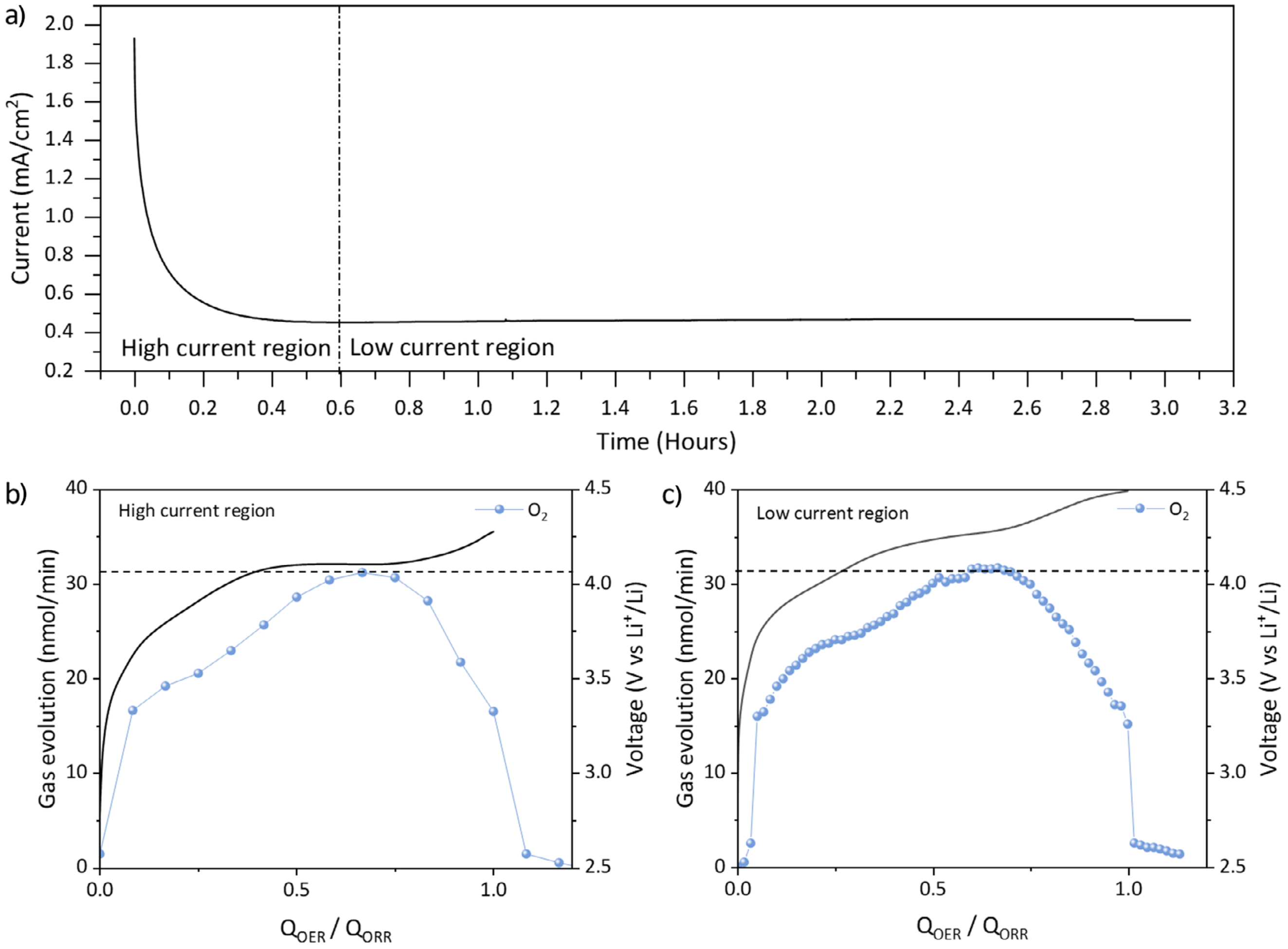

***Figure 4.*** Effect of discharge current on OER efficiency during constant-voltage discharge. a) Discharge profile showing an initial constant-current (CC) step used to remove capacitive contributions, followed by a constant-voltage (CV) step for faradaic discharge. The profile is divided into high-current and low-current regions based on the current response. DEMS results of b) High-current discharge region and c) Low current discharge region. The current density of DEMS charge process is 0.1 mA cm$^{-2}$.

All cells were cycled with voltage cut-off limits set between 2.3 and 4.7 V (Figure S13). The average charging voltage and end discharging voltage versus cycle number are plotted here (Figure 5a). As a result, the 0.1-cell (the cell discharged at 0.1 mA cm$^{-2}$) exhibits the longest cycle life up to 245 cycles. In comparison, the 0.05-cell had 235 cycles and 0.2-cell had 153 cycles (Figure 5b–d). Moreover, while the 0.2-cell exhibited the lowest OER potential in the initial few cycles, after six cycles, the difference was nullified with the 0.2-cell becoming the cell with the high OER potential at the 36th cycle.

Based on previous results, we believe that the cycle performance is affected by several factors. When the discharge voltage of the 0.2 mA cm$^{-2}$ cell drops below 2.30 V at the 163rd cycle (last cycle of 0.2-cell), its corresponding charge voltage is already at 4.56 V whereas 0.05 and 0.1-cells exhibit only −4.52 V (for both). As the OER/ORR efficiency at 0.2 mA cm$^{-2}$ was found to be high, the culprit for the decrease cycling performance likely stems from the anode rather than the cathode. The impedance element $Z_1$ (which we attribute to the Li metal) increases with discharge rates. This indicates that high-rate discharge may lead to increased impedance at the anode. While a high discharge rate can reduce the overpotential of OER at the cathode side, it appears to increase the impedance of the anode, adversely impacting the long-term cycling performance of the cells. High-rate discharge accelerates the increase in impedance at the anode-SSE interface. During cycling, the solid electrolyte interface (SEI) formed from side reactions deteriorates the contact between the anode and SSE, increasing impedance. Additionally, the interface between anode and SSE can be degraded due to an unstable SEI. Such damage on the anode side significantly affects the cycle performance of solid-state LOBs. The 0.05-cell exhibited a sharp discharge voltage decay at the −225th cycle accompanied with a drop-in charging voltage, suggest some degree of shorting from dendritic lithium, whereas the 0.1-cell exhibited a more gradual cell death. As discussed earlier, DEMS yield of low-discharge-rate cells is also lower, accompanied by parasitic reactions that produces byproducts. These side products can be formed from the degradation of SSE. These accumulate within the battery during cycling, eventually leading to its failure.

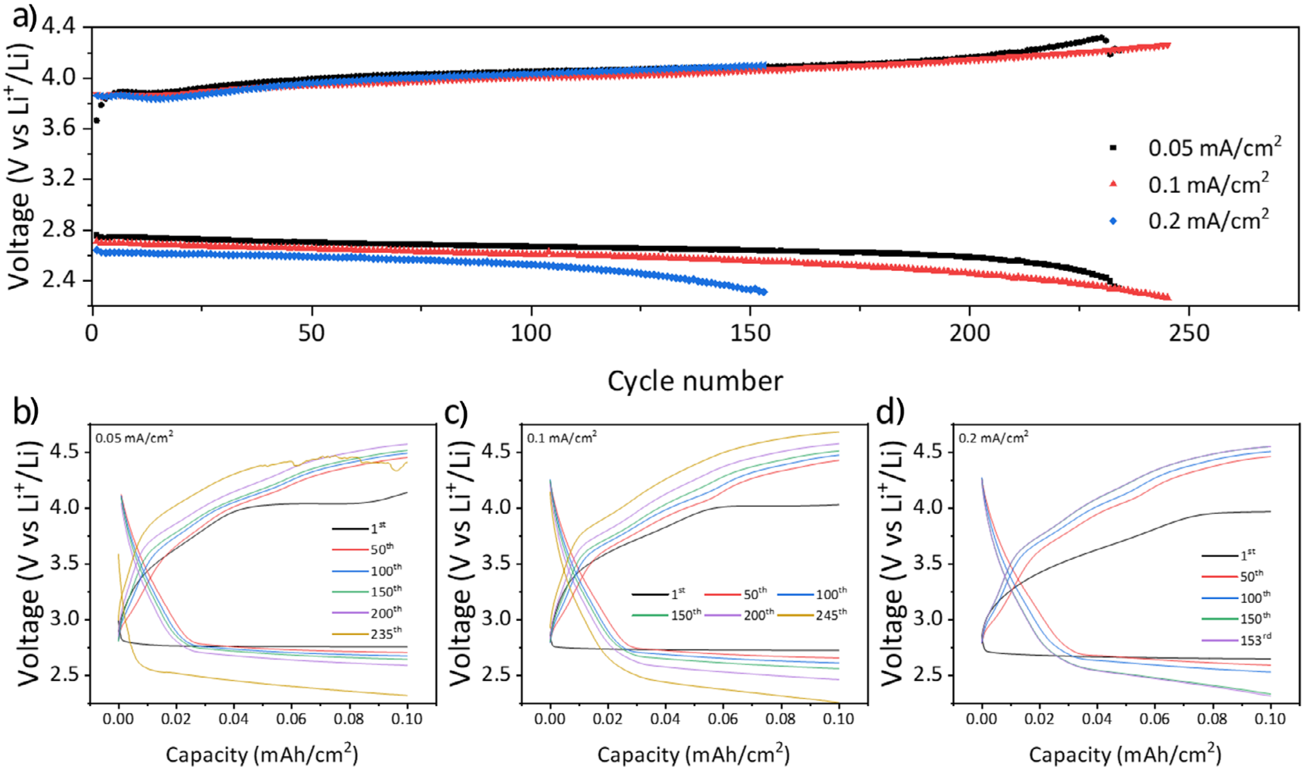

***Figure 5.*** Cycle performance. a) Plot of terminal average charge/discharge voltage versus cycle number of solid-state LOBs discharged at different rates of 0.05, 0.1, and 0.2 mA cm$^{-2}$, and charged at same rate of 0.1 mA cm$^{-2}$. All capacities are 0.1 mAh cm$^{-2}$. b)–d) Voltage profiles of solid-state LOBs discharged at different rates at every 50 cycles until the end of life.

At the beginning of the cycle, high-rate discharge results in a lower charge voltage and overall higher coulombic efficiency based on OER/ORR yields, which is expected to contribute to longer cycle life. However, this trend cannot be maintained throughout cycling due to instability at the anode. Additionally, while our findings align with previous studies on liquid electrolyte system showing that high-rate discharge leads to lower charge voltage, Lu et al. reported a contrasting observation: during the first 75% of the charge process, high-rate discharge resulted in a higher charge voltage, whereas in the final 25%, the trend was consistent with our results.[44] This discrepancy remains unexplored. Clearly, charge voltage is significantly influenced by capacity, byproduct formation, and nucleation or growth phase of $Li_2O_2$. In our work, high-rate discharge is beneficial for having lower charge voltage and higher overall ORR/OER efficiency. However, it causes more damage to the anode surface, resulting in a rapid decay of discharge voltage and significantly shortening the cycle life. While the difference between 0.2 and 0.1 mA cm$^{-2}$ is not typically considered significant for lithium metal battery, we want to point out that such lithium metal cycling conditions in LOB are different than those of a traditional lithium metal anode cell due to the formation dissolution of numerous gas species existing in a LOB cell. Work by Matsuda et al. has shown that cathode/anode crossovers of $O_2$ and $CO_2$/$H_2O$ formed from side reactions unique to LOB are detrimental to the cycling of the lithium metal anode and performance degradation occurs at current densities of a similar order of magnitude (0.4 mA cm$^{-2}$) to our work.[45] Low-rate discharge is advantageous to having lower discharge overpotential and milder effect on the anode but suffers from lower ORR/OER efficiency, resulting in the formation of more side products. These side products degrade the interfaces of each battery component and weaken the contact between the electrodes and the SSE, finally leading to battery failure. In our analysis, a discharge rate of 0.1 mA cm$^{-2}$ is identified as the optimal rate for extending cycle performance.

To evaluate the impact of residual casting solvent (DMF) on the observation and conclusion of this study, two additional SSE films containing different amounts of residual solvent were prepared by varying the drying time. TGA analysis revealed that the residual DMF contents in these SSE films were 18.3% and 30.9%, respectively (Figure S14a,b). Using the two SSE films, deep discharge experiments were performed, and the discharged cathodes were analyzed by SEM to observe the size of the $Li_2O_2$ particles. As shown in Figure S14e,f, a lower discharge rate produced smaller $Li_2O_2$ particles when using the SSE film containing 18.3% residual DMF. A similar trend was observed with the SSE film containing 30.9% residual DMF, as shown in Figure S14g,h. These results confirm that the $Li_2O_2$ particle size still increase with the increase of discharge rate regardless of residual solvent in the SSE film.

In addition, the first-cycle discharge/charge voltage profiles show that cells discharged at higher current densities exhibit lower charge voltages (Figure S15a,e). DEMS analysis revealed that the OER efficiencies for cells using the SSE film with 18.3% residual DMF were 76.1% and 81.1% at discharge current densities of 0.1 and 0.2 mA cm$^{-2}$, respectively (Figure S15c). Similarly, the OER efficiencies for cells using the SSE film with 30.9% residual DMF were 82.0% and 86.2% at 0.1 and 0.2 mA cm$^{-2}$, respectively (Figure S15g). These results demonstrate that the OER efficiency improves with increasing discharge current density, regardless of the residual DMF content in the SSE film. $CO_2$ evolution also increases with higher discharge rates, suggesting that lower discharge rates lead to the formation of more byproducts (Figure S15d,h), which is consistent with our previous observations. For cycling performance, the cell discharged at 0.1 mA cm$^{-2}$ exhibited a longer cycle life than the cell discharged at 0.2 mA cm$^{-2}$, regardless of the residual DMF content in the SSE (Figure S15i,j). This trend is also consistent with our previous observations. All these results exhibit the same trend across SSE films containing different amounts of residual DMF, 18.3%, 23.3%, and 30.9%, confirming that the presence of residual casting solvent (DMF) does not affect the key observations or conclusions of this study.

## Conclusion

This work reveals the impact of discharge rate on the morphology of discharge product, resulting in varying ORR/OER efficiencies and ultimately, different electrochemical performance. It is worth noting that the difference between solid-state LOBs and liquid-state LOBs may change the behavior of electrochemical reactions. $Li_2O_2$ particle sizes were found to increase with increasing current density which contrasts with commonly accepted trends in pure liquid electrolyte system. Compared to liquid-state LOBs, solid-state LOBs have lower ionic conductivity and homogeneity in Li-ion transport and $O_2$ transport. Such limitations might impose a degree of difficulty of Li-ion to nucleate new $Li_2O_2$ rather than simply contributing to the growth of already existing $Li_2O_2$ in established Li-ion conducting paths, unlike the uniform distribution observed in liquid-state LOBs. We propose that the formation of space charge layers leads to the deactivation of less accessible interfacial sites, where limited $Li^+$ and $O_2$ transport prevents effective electrochemical reactions. As a result, only a subset of highly active sites remains electrochemically functional under high-current densities, giving rise to site-selective $Li_2O_2$ growth. This selective behavior is consistent with the spatial heterogeneity at the SSE–cathode interface, as revealed by synchrotron SAXS analysis. The solid-state LOB system consistently exhibits lower charge voltage at high discharge rates like previous studies in liquid-state LOB systems. However, in the solid-state LOB system, the charge voltage is primarily affected by byproducts formed during low-rate discharge, rather than the dimensional size of $Li_2O_2$ as seen in liquid-state LOB systems. In addition, it is found that the efficiencies of both the OER and ORR improve with increasing discharge rate. As a result, in our benchmark, a discharge rate of 0.1 mA cm$^{-2}$ is identified as the optimal rate for extending cycle performance. A low discharge rate promotes the formation of byproducts, while a high discharge rate accelerates the passivation of the anode interface.

## Supporting Information

Supporting information is available. The authors have cited additional references within the Supporting Information.[46,47]

## Acknowledgements

The authors gratefully acknowledge support of this work from the U.S. Department of Energy (DOE), Office of Energy Efficiency and Renewable Energy, Vehicle Technologies Office. Argonne National Laboratory is operated for the U.S. DOE, Office of Science, by UChicago Argonne, LLC, under Contract No. DE-AC02-06CH11357. Use of the Center for Nanoscale Materials, an Office of Science user facility, was supported by the U.S. DOE, Office of Science, Office of Basic Energy Sciences, under Contract No. DE-AC02-06CH11357. Shoichi Matsuda acknowledges support by Japan Science and Technology Agency (JST), Adopting Sustainable Partnerships for Innovative Research Ecosystem (ASPIRE), under Contract No. JPMJAP2309. This research used resources of the Advanced Photon Source (12-ID-B), a U.S. Department of Energy (DOE) Office of Science user facility operated for the DOE Office of Science by Argonne National Laboratory under Contract No. DE-AC02-06CH11357. The authors gratefully acknowledge access to the nGauge atomic force microscope loaned by ICSPI Corp. (Waterloo, Ontario, Canada). [Correction added on 6 August 2025, after first online publication: Acknowledge to the ICSPI Corp. has been insert in the Acknowledgement Section.]

## Conflict of Interests

The authors declare no conflict of interest.

## Data Availability Statement

The data that support the findings of this study are available from the corresponding author upon reasonable request.

**Keywords:** Discharge current density • Lithium oxygen battery • Morphology • Oxygen evolution reaction • Solid-state battery

---

[1] W.-J. Kwak, D. S. Rosy, C. Xia, H. Kim, L. R. Johnson, P. G. Bruce, L. F. Nazar, Y.-K. Sun, A. A. Frimer, M. Noked, S. A. Freunberger, D. Aurbach, *Chem. Rev.* **2020**, *120*, 6626–6683.

[2] M. Balaish, E. Peled, D. Golodnitsky, Y. Ein-Eli, *Angew. Chem. Int. Ed.* **2015**, *54*, 436–440.

[3] H.-D. Lim, H. Song, J. Kim, H. Gwon, Y. Bae, K.-Y. Park, J. Hong, H. Kim, T. Kim, Y. H. Kim, X. Lepró, R. Ovalle-Robles, R. H. Baughman, K. Kang, *Angew. Chem. Int. Ed.* **2014**, *53*, 3926–3931.

[4] J. Chen, A. Gutierrez, M. T. Saray, R. S. Yassar, M. Balasubramanian, Y. Wang, J. R. Croy, *J. Electrochem. Soc.* **2021**, *168*, 080506.

[5] J. Chen, A. Gutierrez, M. A. Sultanov, J. Wen, J. R. Croy, Y. Wang, V. Srinivasan, P. Barai, *ACS Appl. Energy Mater.* **2024**, *7*, 2167–2177.
[6] X. Huang, J. Shea, J. Liu, N. M. Hagh, S. Nageswaran, J. Wang, X. Wu, G. Kwon, S.-B. Son, T. Liu, J. Gim, C.-C. Su, P. Dong, C. Fang, M. Li, K. Amine, U. Jankairaman, *ACS Appl. Mater. Interfaces* **2025**, *17*, 7648–7656.
[7] D. Córdoba, X. Huang, H. B. Rodríguez, M. Li, S.-B. Son, E. J. Calvo, K. Amine, *J. Phys. Chem. C* **2025**, *129*, 3404–3413.
[8] T. Lu, Y. Qian, K. Liu, C. Wu, X. Li, J. Xiao, X. Zeng, Y. Zhang, S.-L. Chou, *Adv. Energy Mater.* **2024**, *14*, 2400766.
[9] X. Yao, Q. Dong, Q. Cheng, D. Wang, *Angew. Chem. Int. Ed.* **2016**, *55*, 11344–11353.
[10] L. Wang, R. Xie, B. Chen, X. Yu, J. Ma, C. Li, Z. Hu, X. Sun, C. Xu, S. Dong, T.-S. Chan, J. Luo, G. Cui, L. Chen, *Nat. Commun.* **2020**, *11*, 5889.
[11] L. D. Griffith, A. E. S. Sleightholme, J. F. Mansfield, D. J. Siegel, C. W. Monroe, *ACS Appl. Mater. Interfaces* **2015**, *7*, 7670–7678.
[12] B. Horstmann, B. Gallant, R. Mitchell, W. G. Bessler, Y. Shao-Horn, M. Z. Bazant, *J. Phys. Chem. Lett.* **2013**, *4*, 4217–4222.
[13] Y. Li, J. Wang, X. Li, D. Geng, M. N. Banis, Y. Tang, D. Wang, R. Li, T.-K. Sham, X. Sun, *J. Mater. Chem.* **2012**, *22*, 20170–20174.
[14] C. Xia, M. Waletzko, L. Chen, K. Peppler, P. J. Klar, J. Janek, *ACS Appl. Mater. Interfaces* **2014**, *6*, 12083–12092.
[15] R. R. Mitchell, B. M. Gallant, Y. Shao-Horn, C. V. Thompson, *J. Phys. Chem. Lett.* **2013**, *4*, 1060–1064.
[16] L. Liu, Y. Liu, C. Wang, X. Peng, W. Fang, Y. Hou, J. Wang, J. Ye, Y. Wu, *Small Methods* **2022**, *6*, 2101280.
[17] N. B. Aetukuri, B. D. McCloskey, J. M. García, L. E. Krupp, V. Viswanathan, A. C. Luntz, *Nat. Chem.* **2015**, *7*, 50–56.
[18] K. He, X. Bi, Y. Yuan, T. Foroozan, B. Song, K. Amine, J. Lu, R. Shahbazian-Yassar, *Nano Energy* **2018**, *49*, 338–345.
[19] J. Wang, Y. Li, X. Sun, *Nano Energy* **2013**, *2*, 443–467.
[20] X. Huang, M. Li, K. Amine, *Renewables* **2024**, *2*, 421–429.
[21] A. Chamaani, M. Safa, N. Chawla, B. El-Zahab, *ACS Appl. Mater. Interfaces* **2017**, *9*, 33819–33826.
[22] H.-F. Wang, D.-H. Guan, X.-K. Chang, X.-Y. Ma, X.-Y. Yuan, X.-X. Wang, J.-J. Xu, *Small* **2025**, *21*, 2411747.
[23] D. Du, H. He, R. Zheng, L. Zeng, X. Wang, C. Shu, C. Zhang, *Adv. Energy Mater.* **2024**, *14*, 2304238.
[24] R. Zheng, D. Du, Y. Yan, S. Liu, X. Wang, C. Shu, *Adv. Funct. Mater.* **2024**, *34*, 2316440.
[25] H. Wong, T. Liu, M. Tamtaji, X. Huang, T. W. Tang, M. D. Hossain, J. Wang, Y. Cai, Z. Liu, H. Liu, K. Amine, W. A. Goddard, Z. Luo, *Nano Energy* **2024**, *121*, 109279.
[26] X. Yu, L. Zhao, Y. Li, Y. Jin, D. J. Politis, H. Liu, H. Wang, M. Liu, Y.-B. He, L. Wang, *ACS Energy Lett.* **2024**, *9*, 2109–2115.
[27] J. Qiu, X. Liu, R. Chen, Q. Li, Y. Wang, P. Chen, L. Gan, S.-J. Lee, D. Nordlund, Y. Liu, X. Yu, X. Bai, H. Li, L. Chen, *Adv. Funct. Mater.* **2020**, *30*, 1909392.
[28] E. Nasybulin, W. Xu, M. H. Engelhard, Z. Nie, S. D. Burton, L. Cosimbescu, M. E. Gross, J.-G. Zhang, *J. Phys. Chem. C* **2013**, *117*, 2635–2645.
[29] S. Wang, X. Wen, Z. Huang, H. Xu, F. Fan, X. Wang, G. Tian, S. Liu, P. Liu, C. Wang, C. Zeng, C. Shu, Z. Liang, *Adv. Funct. Mater.* **2025**, *35*, 2416389.
[30] M. Wu, D. Liu, D. Qu, Z. Xie, J. Li, J. Lei, H. Tang, *ACS Appl. Mater. Interfaces* **2020**, *12*, 52652–52659.
[31] C. Fang, K. Huang, J. Zhao, S. Tian, H. Dou, X. Zhang, *Nano Res.* **2024**, *17*, 5251–5260.
[32] H. Zheng, D. Xiao, X. Li, Y. Liu, Y. Wu, J. Wang, K. Jiang, C. Chen, L. Gu, X. Wei, Y.-S. Hu, Q. Chen, H. Li, *Nano Lett.* **2014**, *14*, 4245–4249.
[33] L. Johnson, C. Li, Z. Liu, Y. Chen, S. A. Freunberger, P. C. Ashok, B. B. Praveen, K. Dholakia, J.-M. Tarascon, P. G. Bruce, *Nat. Chem.* **2014**, *6*, 1091–1099.
[34] J. Li, J. Chen, X. Xu, Z. Wang, J. Shen, J. Sun, B. Huang, T. Zhao, *Adv. Energy Mater.* **2025**, *15*, 2402746.
[35] C. Prehal, A. Samojlov, M. Nachtnebel, L. Lovicar, M. Kriechbaum, H. Amenitsch, S. A. Freunberger, *Proc. Natl. Acad. Sci. USA* **2021**, *118*, e2021893118.
[36] B. D. Adams, C. Radtke, R. Black, M. L. Trudeau, K. Zaghib, L. F. Nazar, *Energy Environ. Sci.* **2013**, *6*, 1772–1778.
[37] J. Shea, X. Huang, M. Li, S.-B. Son, C.-C. Su, T. Liu, P. Dong, A. Chen, L. Yang, C. Luo, K. Amine, U. Janakiraman, *J. Electrochem. Soc.* **2024**, *171*, 020528.
[38] J. Adams, M. Karulkar, V. Anandan, *J. Power Sources* **2013**, *239*, 132–143.
[39] I. Landa-Medrano, I. Ruiz de Larramendi, N. Ortiz-Vitoriano, R. Pinedo, J. Ignacio Ruiz de Larramendi, T. Rojo, *J. Power Sources* **2014**, *249*, 110–117.
[40] J. Højberg, B. D. McCloskey, J. Hjelm, T. Vegge, K. Johansen, P. Norby, A. C. Luntz, *ACS Appl. Mater. Interfaces* **2015**, *7*, 4039–4047.
[41] L. A. Huff, J. L. Rapp, L. Zhu, A. A. Gewirth, *J. Power Sources* **2013**, *235*, 87–94.
[42] S. J. Folkman, J. González-Cobos, S. Giancola, I. Sánchez-Molina, J. R. Galán-Mascarós, *Molecules* **2021**, *26*, 4756.
[43] Z. Liang, Y.-C. Lu, *J. Am. Chem. Soc.* **2016**, *138*, 7574–7583.
[44] Y.-C. Lu, Y. Shao-Horn, *J. Phys. Chem. Lett.* **2013**, *4*, 93–99.
[45] S. Matsuda, M. Ono, H. Asahina, S. Kimura, E. Mizuki, E. Yasukawa, S. Yamaguchi, Y. Kubo, K. Uosaki, *Adv. Energy Mater.* **2023**, *13*, 2203062.
[46] P. Martins, A. C. Lopes, S. Lanceros-Mendez, *Prog. Polym. Sci.* **2014**, *39*, 683–706.
[47] X. Zhang, T. Liu, S. Zhang, X. Huang, B. Xu, Y. Lin, B. Xu, L. Li, C.-W. Nan, Y. Shen, *J. Am. Chem. Soc.* **2017**, *139*, 13779–13785.

Manuscript received: April 09, 2025
Revised manuscript received: July 01, 2025
Accepted manuscript online: July 15, 2025
Version of record online: August 01, 2025